WIND TUNNEL TEST AND AEROELASTIC MODEL VALIDATION OF ELECTRICAL LIFT-THRUST UNITS

Davide Balatti, Michal Szydlowski, Leonardo Helicopter, Yeovil, UK
Michele Zilletti, Andrea Duina, Leonardo Helicopters, Samarate, Italy
Enrico Sabatino, Leonardo Helicopters, Pisa, Italy
Pierangelo Masarati, Politecnico di Milano, Milano, Italy

Abstract

The increasing interest in multi-propeller electric Vertical Take-Off and Landing aircraft for Advanced Air Mobility has underscored the need for high-fidelity methodologies capable of predicting and analysing complex aerodynamic and structural interactions across a broad frequency range. These interactions are particularly influenced by the variable rotor speed control strategies typically adopted by Lift Thrust Units. Building on previous experimental work, where the aeroelastic model of one and two grounded LTUs was statically validated, this paper employs roving hammer tests and operational modal analysis to identify, and subsequently incorporate into the aeroelastic model, an elastic representation of the LTU support system. The proposed model aims to enhance the correlation between numerically predicted dynamic loads and wind tunnel measurements over a range of operational conditions. Specifically, the paper investigates how the elastic support influences the system's dynamic response and enhances agreement with experimental measurements. Furthermore, the study considers the effect of rotor phase synchronization and demonstrates its significant impact on the loads generated.

1. ACRONYMS

AAM	Advanced Air Mobility
CFD	Computational Fluid Dynamics
DEP	Distributed Electric Propulsion
EMA	Experimental Modal Analysis
eVTOL	electric Vertical Take-Off and Landing
FE	Finite Element
FFT	Fast Fourier Transform
LTU	Lift/Thrust Unit
MTB	Multirotor Test Bed
NR	Newton-Raphson
OMA	Operational Modal Analysis
RPM	Revolutions Per Minute
RVLT	Revolutionary Vertical Lift Technology
SDOF	Single Degree Of Freedom
SSI	Stochastic Subspace Identification
VVPM	Viscous Vortex Particle Method

2. INTRODUCTION

The advent of electric propulsion has enabled new design opportunities in flight vehicles, thanks to compact, efficient electric motors and energy-dense battery systems. These technologies have paved the way for the emergence of electric Vertical Take-Off and Landing (eVTOL) aircraft. Both major aerospace companies and smaller firms are increasingly investing in new Distributed Electric Propulsion (DEP) aircraft design, such as multicopters, tilt-wing aircraft, tilt lift-thrust systems, and coaxial multirotors for Advanced Air Mobility (AAM), cargo transport, and military missions.

NASA's Revolutionary Vertical Lift Technology (RVLT) project has defined reference configurations for eVTOL aircraft and has assessed propulsion strategies, control logic, and performance trade-offs across multiple designs [1, 2]. These studies have shown that DEP architectures promise multiple advantages over conventional rotorcraft: enhanced safety via propulsion redundancy, the potential for zero-emission operations, simplified mechanical architecture (e.g., elimination of gearboxes and swashplates), and direct motor speed control of rotors [3, 4]. In particular, lift/thrust units (LTUs) with fixed-pitch blades and variable-speed electric drives can significantly simplify mechanical design and system integration.

However, these benefits introduce new technical challenges in terms of control authority, dynamic stability, failure resilience, and structural loading. In contrast to traditional helicopters where articulated rotors attenuate dynamic loads at the hub, rigid LTUs, operating at continuously variable rotor speeds, may excite resonances across a wide frequency spectrum. Such excitations can amplify vibrations particularly in edgewise flight conditions [5, 6]. These dynamics are further complicated by the aerodynamic interference and wake coupling effects of multiple rotors [7].

To support early-stage design decisions, NASA has developed the modular Multirotor Test Bed (MTB) [8, 9] for evaluating multi-LTU performance under dynamic and realistic inflow conditions reproduced in the wind tunnel. This setup is fully reconfigurable, allowing each LTU to be independently tilted and moved horizontally and vertically. Each LTU was equipped with a load cell to measure the six load components in the fixed reference frame. Sekula et al. [5] conducted a parametric study on the LTU transient response, validating analytical models with NASA's experimental data and emphasizing the importance of rotor wake model and blade elasticity properties. More recently, Conley et al. [10] focused on a quadrotor configuration tested with NASA's MTB, investigating the effects of rotor placement, blade number, and rotor phasing. They examined both the quasi-steady and dynamic loads generated by the rotors and concluded that certain dynamic load components are significantly dependent on the rotor phase.

Staruk et al. [3] tested a single full-scale two-blade LTU (1.8 m diameter) in a wind tunnel, observing high dynamic loads generated by the LTU in edgewise rotor airflow conditions compared to the static counterpart due to the excitation of the rotor modes.

Zilletti et al. [11] designed and tested a setup to characterize the static and dynamic behaviour of an electrical LTU. Their results showed that a stiff rotor can generate high oscillatory loads in edgewise airflow conditions, with magnitudes comparable to the corresponding static loads. The test rig was expanded to study the interaction of two LTUs under various flight conditions and configurations mainly focusing on static aerodynamic loads [12].

This paper uses the data collected in the previous wind tunnel test campaign [12] to assess and model the dynamic interaction between the LTUs and the supporting structure.

The objectives of the paper are:

1. To combine Experimental Modal Analysis (EMA) and Operational Modal Analysis (OMA) to identify a structural dynamic model able to describe the complex structure/propellers interactions in the blade passing frequency band.
2. To evaluate the amplification of the loads and vibration given by the presence of rotor and structural resonances.
3. To validate Leonardo's comprehensive GyroX code with experimental data.

Section 3 describes the rig architecture and provides an overview of the data collected during the tests; Section 4 details the implementation of the in-house software GyroX, the model and the methodology used to identify a structural model. The correlation between experimental and simulated oscillatory loads is presented in Section 5. Conclusions are drawn in Section 6.

3. EXPERIMENTS

3.1. Rig Description

Figure 1 shows a picture of the wind tunnel test rig consisting of two LTUs arranged in tandem, supported by an aluminium beam. The supporting structure is mounted on a pylon, which allows to tilt the beam in the wind direction. The two thrust units can be independently moved along the supporting structure to adjust the distance between the propellers. Each LTU consists of a 3-blade fixed pitch propeller, approximately 0.6 meters in diameter, driven by an electric motor. A more detailed description of the test rig can be found in Reference [12]. Each LTU is mounted on a 6-axis load cell able to measure both the static and oscillatory loads (3 forces and 3 moments) exchanged between the structure and the LTU. Two 3-axial accelerometers are mounted on the structure close to the LTUs during the wind tunnel test.

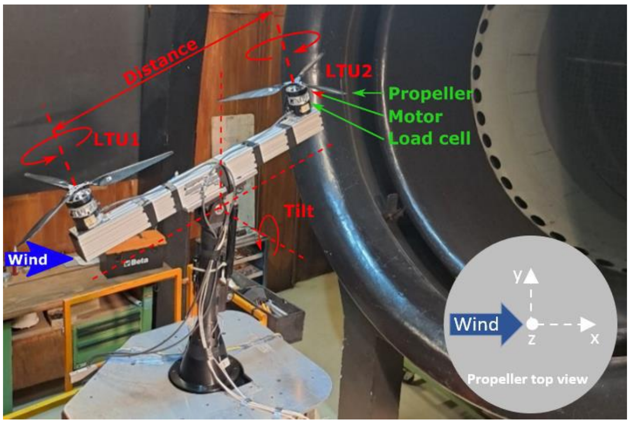

Figure 1: Wind tunnel test rig.

3.2. Experimental Wind Tunnel Data

The full test campaign consisted of 168 conditions, comprising no wind and 18 m/s wind speed conditions, 3 tilt angles, 3 LTU distances (symmetrically positioned along the beam), and 14 rotor speed steady-state regimes, as detailed in Reference [12]. Moreover, RPM ramps to both LTUs were performed to be used for OMA.

In this study, the analysis was limited to measurements obtained in the configuration with 0° tilting, a freestream wind speed of 18 m/s, and a spacing between LTU centres equal to 1.4 rotor diameters.

3.3. Structural Dynamics Characterization Test

To characterise the dynamics of the rig structure, hammer roving tests were conducted. Six triaxial accelerometers were placed on the structure:

- Two at the base of each LTU,
- Two on the supporting structure directly beneath the load cells,
- One at the base of the pylon,
- One on the tilting mechanism.

Hammer input excitations were given at the accelerometer locations in all three directions, where possible. Additionally, a separate roving hammer test was performed on the support beam structure in free-free conditions, with the load cell – LTU assemblies in place. Together, these tests enabled the modal identification of both the complete rig and the support structure.

4. GYROX MODEL

In a previous paper, Zilletti et al. [11] presented the propeller definition and characterization, as well as the validation of the GyroX model for a single LTU. This work was extended by Balatti et al. [12] to the case of two LTUs focussing on the aerodynamic interaction and quasi-static load generation mechanism. The following section provides an overview of GyroX and the modelling approach to predict the oscillatory loads.

4.1. GyroX Software Implementation

GyroX is an in-house simulation tool developed by Leonardo Helicopters, designed to deliver fast and reliable numerical solutions for aeroelastic and aeromechanical analyses of complex rotorcraft systems. Ongoing development of GyroX aims to establish it as a multi-comprehensive platform for aircraft design and analysis.

The equations of motion governing the mechanical system are assembled and numerically solved within GyroX. In contrast, the aerodynamic forcing terms acting on the system are evaluated separately by an external solver, which is coupled to GyroX to ensure consistent representation of the aeroelastic interactions. In the present study, aerodynamic loads are computed using the built-in module AeroX, which offers a versatile suite of analytical and scalable mid-fidelity methods for aerodynamic modelling, such as the vortex lattice and the viscous vortex particle method (VVPM) (more details on the aerodynamic methods are presented in [13]).

Once the model is assembled, various analyses can be performed to address several types of problems. Under the assumption of periodicity, the steady-state response can be obtained directly in the frequency domain, while the transient response is evaluated through time-domain numerical integration of the equations of motion. The stability characteristics of the system can be assessed in either the rotating or fixed reference frame, using appropriate methods such as the mean matrix approach or Floquet theory. The elastic blades are modelled using a geometrically exact Total Lagrangian beam formulation, discretized via the Finite Element Method.

In this study, the steady-state response is computed by reformulating the problem in the frequency domain and solving the non-linear equilibrium equations iteratively by using the incremental Newton-Raphson (NR) method (incremental load stepping method [14]). Hence, the aerodynamic forcing is introduced progressively over multiple steps; each time an intermediate solution is found, a new aerodynamic evaluation is performed (based on the updated displacement/velocity field), until 100% of the load is applied. The aerodynamic solver operates in the time domain using an independently selected time step, carefully chosen to balance convergence and accuracy. After the aerodynamic integration attains steady state, the loads are sampled over a predefined time window and then transformed in the frequency domain by the Fast Fourier Transform (FFT).

To enhance the robustness of the Newton–Raphson procedure, aerodynamic derivatives are also computed and incorporated into the system's gradient. These derivatives capture the sensitivity of lift and drag to changes in blade strip displacement and velocity. However, they do not account for the influence of variations in induced velocity on the aerodynamic loads. While this simplification is acceptable for ensuring numerical convergence, it may reduce accuracy when assessing stability characteristics. In such cases, more precise modelling approaches may be necessary. The gradient has been derived in closed form in the frequency domain, following the approach outlined in [15].

The degrees of freedom associated with the blades are formulated in the rotating reference frame, while those of the stationary structure are defined in the fixed (inertial) frame. To ensure consistent interaction between these two subsystems, a kinematic constraint is applied at their interface. This constraint enforces displacement compatibility, effectively tying the motion of the interface point in both frames. Additionally, it ensures dynamic equilibrium by transmitting the reaction forces and moments between the rotating and fixed domains.

To enhance computational efficiency, the code is parallelized using OpenMP. In detail, both the residual and the system gradient in the frequency domain are evaluated in parallel across the discrete time samples. This parallelization strategy significantly reduces the computational time of each Newton-Raphson iteration, especially for finely discretized periods, making the approach suitable for complex rotorcraft configurations and large-scale simulations. Once the NR gradient is computed, it is inverted via the direct sparse solver PARDISO [16]. Also concerning the aerodynamic implementation, the parallelization strategy has been discussed in [13].

4.2. LTU Aeroelastic Model

In the aeroelastic model defined in Reference [12], both LTUs share the same structural and aerodynamic model. The only difference between the two LTUs is the rotation direction (looking from the top view, the front rotor rotates counterclockwise and the rear one clockwise). A more detailed description of the LTU's model can be found in Reference [11]. The airfoil geometry was obtained through 3D blade scanning, and the aerodynamic coefficients (lift, drag, and pitching moment) were defined as functions of the airfoil angle of attack and Mach number. To create look-up tables for these coefficients, a 2D quadrilateral O-grid mesh was generated using Pointwise®, with pressure far-field boundary conditions and adiabatic wall conditions on the airfoil surface. SST k-ω turbulence models were employed for simulations conducted with Ansys Fluent® at a Reynolds number over Mach number of 6,256,000. The aerodynamic coefficients were then formatted according to the C81 table standard.

Each blade is modelled using 22 beam elements with cubic shape functions, as shown in Figure 2 (the blue spherical markers represent the nodes between the beam elements). The three blades are connected to a shaft via three very rigid beams representing the rotor hub. The shaft is modelled as a rigid element with one terminal connected to the rotor hub centre and the other to the ground. Using the CFD-based C81 tables, a Lifting Line free wake model was selected for the aeroelastic simulation.

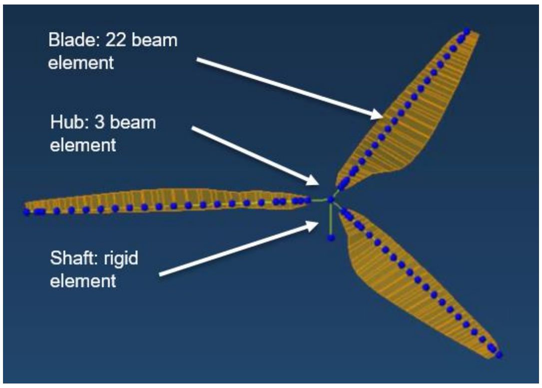

Figure 2: GyroX rotor model.

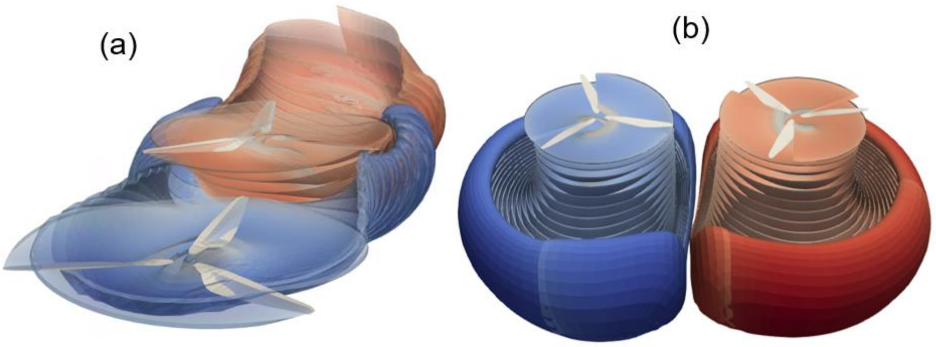

Figure 3: Typical aerodynamic solution in tandem configuration, 0° tilting angle and spacing between LTU centres equal to 1.1 rotor diameters (a) at 18 m/s, with the wake of the front LTU investing the rear LTU and (b) in hover, with the first vortex rolling up, and the near-wake narrowing just under the rotor plane.

The distribution of the aerodynamic control nodes was made of 30 points with geometrical progression and refinement at the tip. The aerodynamic model was set up so that the aerodynamics and wake of each LTU interact with those of the other one. For each configuration, the appropriate number of rotor revolutions was carefully determined to ensure that the loads reached a steady-state condition, accounting for the specific aerodynamic interactions between the rotors. Figure 3a presents a typical aerodynamic solution for the LTUs in a tandem configuration at 0° tilt angle, 18 m/s wind speed and a spacing between LTU centres equal to 1.1 rotor diameters, with the wake of the front propeller investing the rear one. Figure 3b shows the aerodynamic solution in hover with the first vortex rolling up and the near-wake narrowing just under the rotor plane.

4.3. Structural Model Identification

This section presents the modelling approach used to account for the dynamic effects of the supporting structure on the oscillatory loads generated by the two LTUs. The strategy involves the progressive enrichment of the structural model by incorporating the dynamics of additional components and evaluating their influence on the oscillatory loads prediction. Figure 4 schematically illustrates the three models considered.

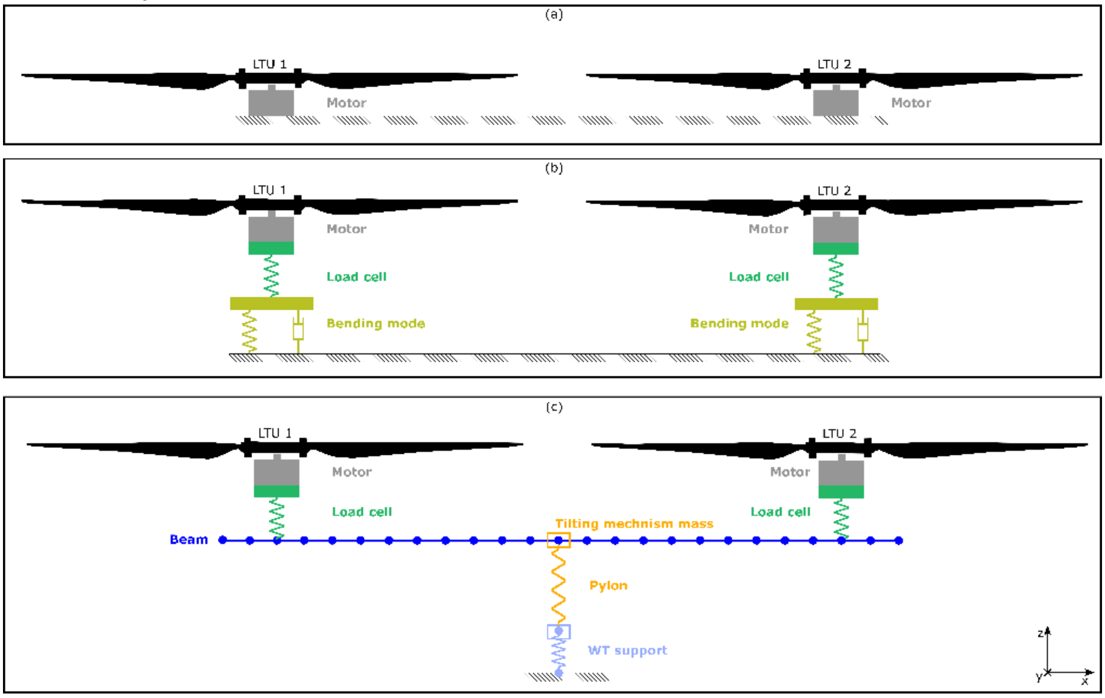

Figure 4: Lumped parameter models of the test rig consisting of: (a) two grounded LTUs, (b) LTUs, load cells and first bending structural mode, (c) LTUs, load cells, supporting beam and WT stand.

Model (a) is the simplest configuration, consisting of two LTUs (modelled as described in Section 4.2), where the structural dynamics are entirely neglected.

Model (b) includes the dynamics of the load cell, represented as a 6-degree-of-freedom (DOF) spring–mass system, and the first bending mode of the supporting beam modelled as single DOF system oscillating in z-direction. Although this model captures aspects of both structural and load cell dynamics, the two LTUs remain dynamically independent. While the masses used in the model are known, the stiffness properties of the load cells were estimated through shake tests, as described in [12]. The properties of the first bending mode were identified using EMA data.

Finally, Model (c) is the most detailed configuration, consisting of:

- The load cells – LTU assemblies of Model (b).
- The supporting beam modelled by 50 beam finite elements (blue line in Figure 4 (c)).
- The pylon, modelled as a 6-DOF spring and a lumped mass to account for the mass and inertia of the beam–pylon attachment mechanism (yellow line in Figure 4 (c)).
- The wind tunnel stand, modelled as a 6-DOF spring and a lumped mass (light blue line in Figure 4 (c)).

Given the increased complexity of Model (c) and the broad frequency range associated with the blade-passing frequency, a more refined and structured parameter estimation strategy was adopted. The model identification focused on representing the rig dynamics in the frequency range excited by the 3/rev component over 20–100% RPM. The tuning procedure of Model (c)'s parameters can be split into 4 steps.

Step 1. An initial finite element (FE) model of the beam with the two load cells-LTU assemblies (without the propellers) has been developed. Using the known geometry and material properties of the beam, along with the mass properties of the motors, an initial parameter estimation of the model has been carried out. Furthermore, the results of free-free hammer tests have been used to finely tune the model parameters.

Step 2. The EMA data have been used to extract the natural frequencies and mode shapes from the hammer roving tests performed onto the entire test rig, ranked based on their contribution to the total LTU displacement. Figure 5 shows as an example two FRFs between the excitation force in z-direction applied at LTU1 location and the acceleration along z-axis measured at the mounting points of LTU1 (solid line) and LTU2 (dashed line). The blue vertical lines indicate the natural frequencies identified from the test. Additionally, the mass normalised mode shapes extracted using EMA were used to calculate the averaged normalised unit displacement at the LTU mounting points for each mode and plotted in the bar plot of Figure 6. The graph shows that the four most significant displacement contributions are produced by modes 4, 11, 7, and 3 at about 0.2, 0.88,

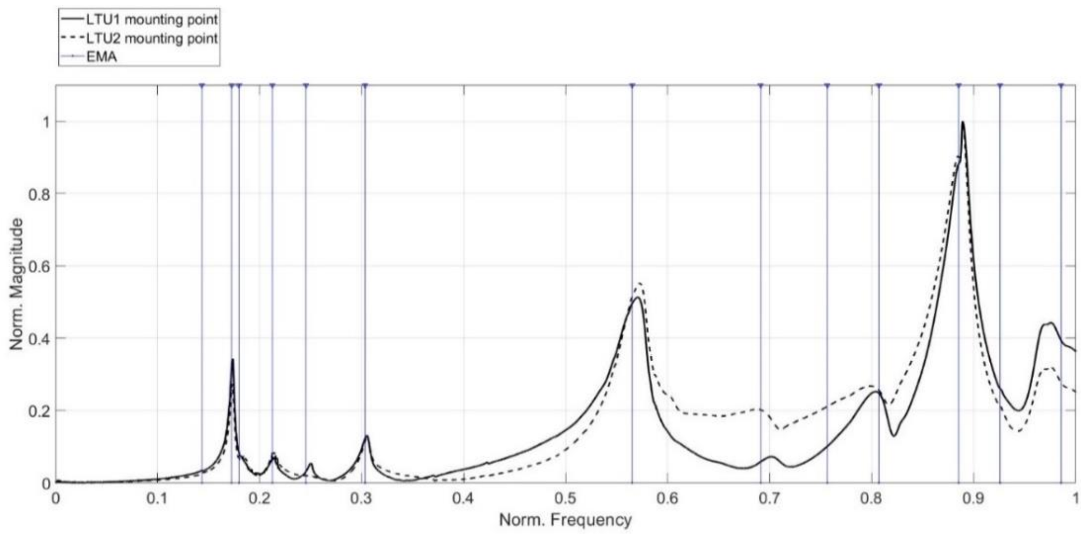

Figure 5: EMA results: FRF's in z-axis of the LTU mounting points with excitation in the z direction. Blue vertical lines show all modes identified during EMA testing of the rig.

normalised frequencies. The mode shapes associated with these natural frequencies are shown in Appendix A and summarised in Table 1.

Table 1: List of four modes contributing most to the LTU base displacement.

Mode	Frequency.	Mode description
4	0.2	Rotation of the support structure around the mounting point on the pylon.
11	0.88	Symmetric vertical bending of the support structure.
7	0.56	Coupled antisymmetric vertical bending of the support structure with longitudinal motion of the pylon.
3	0.18	Coupled lateral-longitudinal motion of the whole rig.

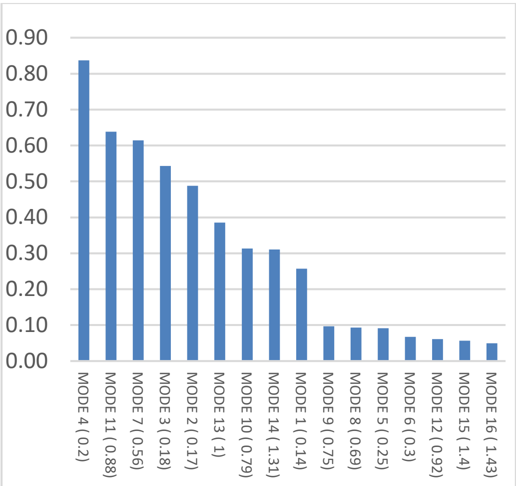

Figure 6: Averaged normalised unit displacement at the LTU mounting points, obtained from EMA.

Step 3. OMA data acquired using the same accelerometers used for EMA when the two LTUs were performing an RPM ramp have been used to identify the mode shapes and natural frequencies in operational conditions. This allowed to:

1. Highlight any difference between the modes and natural frequencies identified with the EMA. This could suggest activation of nonlinear behaviour of the structure, for example induced by the operative loads.
2. Highlight mode interactions.
3. Identify the minimum model order from the model.

The stabilization diagram is a key tool in the SSI-OMA method for extracting modal parameters from output-only vibration data. Figure 7 shows the stabilization diagram obtained from the RPM ramp test. The green dots show the identified poles for each frequency as functions of the model order. Stable poles, those that persist with consistent frequency, damping ratio, and mode shape as the model order increases, indicate true physical modes. In contrast, unstable or spurious poles (often due to noise or numerical artefacts) that vary significantly with model order are discarded.

The black and grey lines show the first and high order singular values of the cross-spectral density matrix of the measured output signals. These singular values indicate how much energy is present at each frequency.

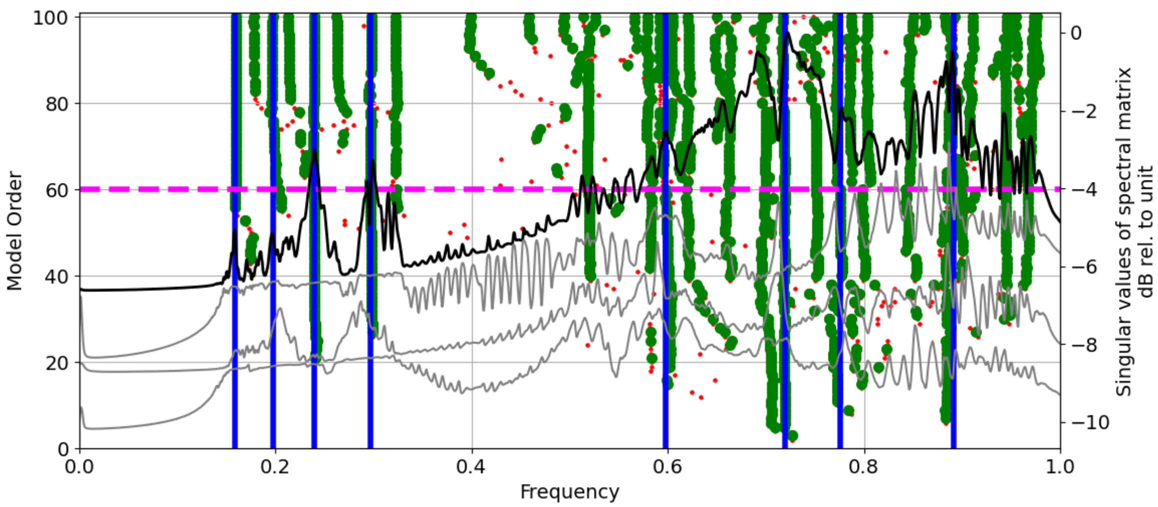

Figure 7: OMA SSI stabilization diagram of two LTU rotor speed ramp test with wind 18 m/s in the tandem configuration. Green points depict stable poles in frequency, mode shape and damping. Black and grey curves depict singular values of spectral matrix. Blue lines indicate selected modes while dashed magenta line shows the selected model order.

- The black line corresponds to the first (largest) singular value, showing the most dominant dynamic responses of the system. Peaks in this curve align with well-excited structural modes.

- The grey lines represent higher-order singular values, which may reveal additional modes, including less dominant or more spatially localised ones.

If a green pole cluster aligns with a peak in the singular values, it strongly suggests a physical mode. If there is no peak in the singular values at a pole location, it may indicate a numerical artefact or weakly excited mode. If the same peak is found in most singular values, it may suggest the presence of a harmonic excitation at that frequency. Blue lines indicate the chosen SSI-OMA modes at model order 60. Other pole clusters visible in the stabilisation diagram were discarded, due to unphysical damping values or mode shape similarity to their neighbours. In this case, OMA and EMA results show similar modal proprieties.

Step 4. Both the pylon (including the tilting mechanism) and the wind tunnel stand were modelled as six-degree-of-freedom (6-DOF) spring elements with associated lumped masses. All the spring stiffness characteristics were tuned to represent the dynamics of the test rig. In the tuning process, the first four modes from the bar chart were prioritised so that the mode shapes and frequencies reflected the OMA/EMA results. The remaining modes were only matched in frequency.

5. DYNAMIC LOADS CORRELATION

In this section, the correlation between experimental measurements and simulation results is evaluated for the oscillatory loads at the 3/rev frequency.

Figure 8 shows the amplitude of the oscillatory vertical force F_z (top plots), rolling and pitching moment M_x and M_y, (middle and bottom plots, respectively) at the load cell location, as functions of the rotor speed percentage. The shear forces F_x and F_y are generally negligible and are therefore omitted.

The plots on the left correspond to the front LTU, while those on the right correspond to the rear one. The black lines represent the measured oscillatory loads obtained during wind tunnel tests at 18 m/s, with both LTUs operating in a tandem configuration. Measurements were taken over a 30 s interval at a constant nominal rotor speed for both LTUs.

In this work, forces and moments are normalized with respect to the simulated static thrust and torque of the front rotor at 100% rotor speed. Accelerations are normalized relative to the maximum simulated dynamic acceleration of the front rotor, obtained using the model with an elastic beam and pylon support.

The amplitude of the experimental oscillatory loads was calculated by averaging the amplitude of the 3/rev harmonic over 50 revolutions windows. The error bars indicate the standard deviation across these intervals, with most of the variation attributed to uncontrolled phase differences between the front and rear rotors during the test as discussed in the next subsection.

The black lines exhibit multiple peaks at different rotor speeds, indicating the presence of several resonances involving the fixed structure and the two propellers. Additionally, noticeable differences between the front and rear rotors suggest interaction between the two LTUs, primarily due to structural dynamic coupling, as will be discussed later.

The blue lines in Figure 8 show the oscillatory loads simulated using Model (a), which consists of two grounded LTUs with no structural coupling. Comparing the left and right plots, the loads on the front and rear LTUs are nearly identical, indicating that aerodynamic coupling (since the LTUs are structurally independent in Model (a)) has a negligible effect on the generation of oscillatory loads. Two prominent peaks are observed in the simulation: one around 38% rotor speed, visible in the F_z component, and another around 50%, evident in the M_x and M_y. This load amplification can be explained using the in-vacuum Campbell diagram of the grounded rotor shown in Figure 9. The diagram reveals that the propeller exhibits a collective flap mode resonance at 3/rev near 38% rotor speed, which amplifies the thrust oscillation, and a cyclic mode resonance at 2/rev near 50% rotor speed, leading to increased rolling and pitching moments. While these peaks are also present in the experimental data (black lines), several additional peaks observed in the measurements are not captured by this simplified model.

The magenta lines in Figure 8 represent the oscillatory load amplitudes simulated using Model (b) and calculated by introducing the load cell model. The

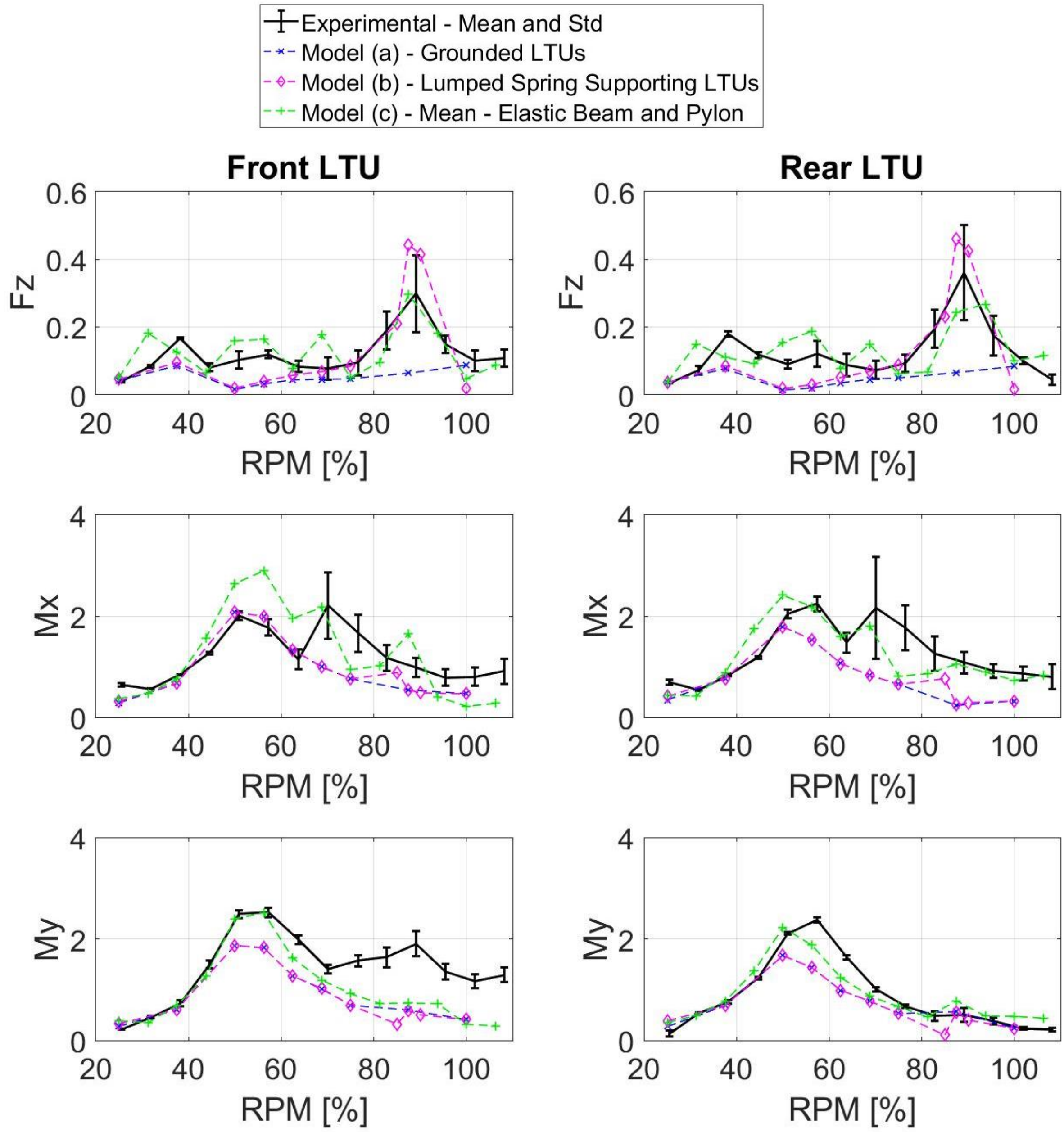

Figure 8: Dynamic forces and moments as functions of rotor speed: measured mean and standard deviation (black line); simulated grounded LTUs (blue line); simulated LTUs supported by isolated springs (magenta line); and mean simulated LTUs supported by the elastic beam-pylon model with different front and rear rotor phases (green line).

main difference compared to Model (a) is the inclusion of the first bending mode dynamics of the supporting beam. This added structural flexibility introduces a resonance that amplifies the F_z oscillation around 90% rotor speed, although the magnitude is overestimated. As in Model (a), the front and rear LTUs produce nearly identical loads, since in this configuration they remain structurally decoupled.

Finally, the green lines represent the simulated loads obtained using Model (c). In this case, since the relative rotor phase affects the resulting loads, the mean value is presented. The impact of rotor phase is discussed in Section 5.1. Notable differences appear between the front and rear LTUs due to structural coupling and the asymmetry of the supporting structure introduced by the beam-to-pylon attachment mechanism. The plots reveal the

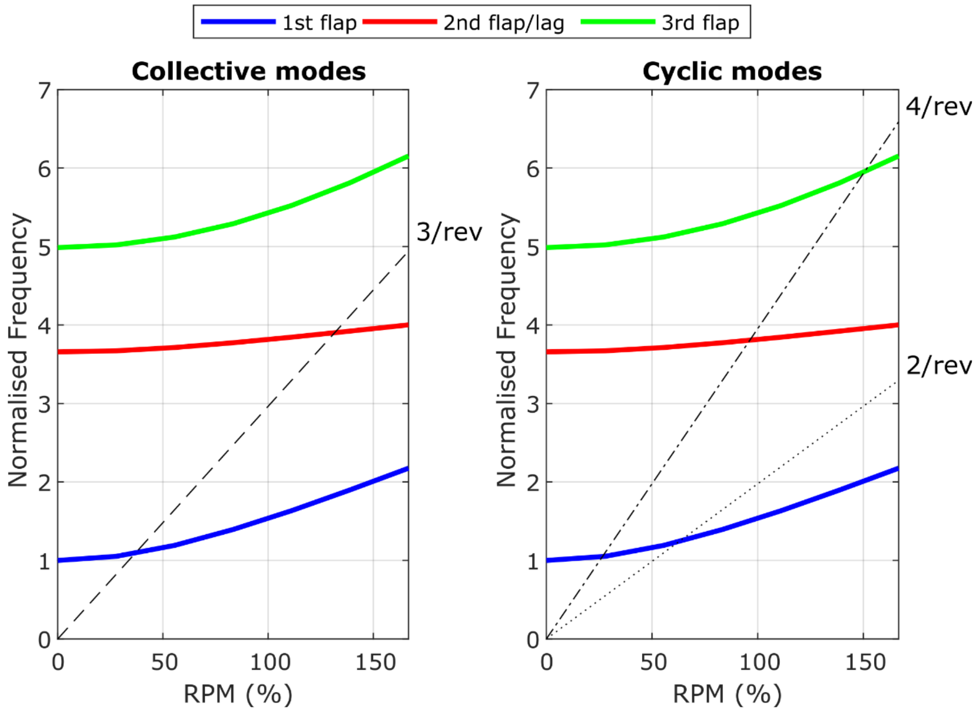

Figure 9: First three collective (left) and cyclic (right) normalised (to the 1st resonance) resonance frequencies of the propeller as a function of the RPM (%). The dotted, dashed and dashed-dotted lines represent the 2/rev, 3/rev, and 4/rev frequencies.

emergence of several peaks corresponding to the excitation of structural modes, as identified in the previous section. Notably, the inclusion of the full structural dynamics in Model (c) results in a better match with the measured amplitude of the oscillatory F_z around 90% rotor speed. Similarly, at around 70% rotor speed, the simulated M_x accurately captures the peak arising from the interaction between the longitudinal pylon mode and the first rotor cyclic mode.

Both front and rear LTUs show elevated values of M_y between 50% and 60% of the rotor speed. Although both models (a) and (b) are able to predict this trend, the model incorporating structural elasticity better matches the experimental behaviour due to a dynamic interaction between the rotor and the supporting structure.

Above 70% of the rotor speed, all simulation results closely match the rear LTU measurements. While simulations show similar trends between the models and between the front and rear LTUs, the experimental data from the front LTU displays a different trend. This discrepancy is likely due to an unmodelled asymmetry in the beam that supports the LTUs.

To summarise, Figure 8 demonstrates that progressively refining the structural model supporting the LTUs improves correlation with experimental data. This improvement stems from the model's enhanced ability to capture the interaction between the rotor and the supporting structure.

5.1. Influence of the Rotor Phase

The relative phase between the front and rear rotors was not controlled during the tests, resulting in a varying phase shift between the loads generated by the two LTUs. This phase difference can cause constructive or destructive interference and beating, depending on rotor speed, phase relationship and specific load components. In real applications, such lack of syncronization would be inevitable when LTUs are independently actuated for flight control purposes.

Figure 10 shows an example of the experimental time history at 90% rotor speed, showing the relative phase between the rotors and the measured thrust on the front and rear LTUs. Due to the interaction between the LTUs and the supporting structure, the constant phase drift leads to a variation in the measurements. This effect is clearly visible in the experimental data: phase drift between the two LTUs during a single test leads to variations in the measured loads, as indicated by the error bars in Figure 8. Figure 11 compares the experimental loads (black lines with error bars) to the simulated load amplitudes for various relative phase angles, as indicated in the figure legend. The results show a clear dependence of the oscillatory load amplitudes on rotor phasing, with the effect becoming more pronounced at specific rotor speeds. This sensitivity is particularly evident at 90% rotor speed, where the amplitude of F_z shows significant variation. At this condition, the first bending mode of the structure (Mode 11, shown in Appendix A) is strongly excited when the two rotors are in phase, due to the mode shape's symmetry, and weakly excited when they are in opposite phase.

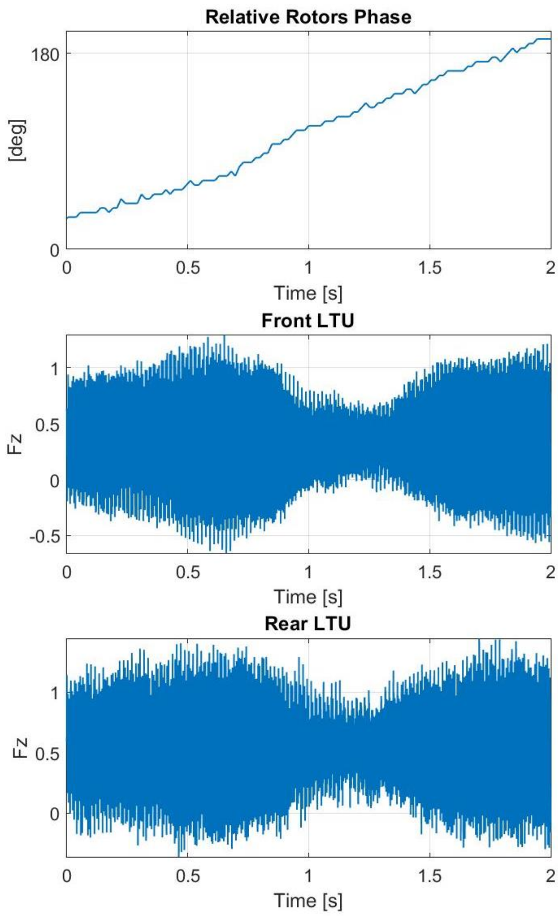

Figure 10: Experimental time history of rotor relative phase and front and rear LTU thrust at 90% rotor speed.

Similarly, the experimental F_z shows high variability around 50% rotor speed, where the first cyclic rotor mode interacts with Mode 7 (shown in Appendix A). However, this variability is less significant in the experimental measurements. The discrepancy is likely due to an overestimation of the vertical displacement of the LTUs in the mode shapes of Mode 7.

The variability in M_x at 70% rotor speed, probably due to a combination of Modes 11 and 7, is accurately predicted. Thanks to the correct representation of the lateral displacement of these two modes, the simulation successfully captures the lower variability of the front LTU compared to the rear one.

At 90% rotor speed, the simulation results exhibit greater variability in M_x compared to the experimental measurements. This discrepancy is likely due to an overestimation of the beam rotation associated with Mode 11. Both measurements and simulation results for the front and rear LTUs indicate low variability in the M_y moment. Furthermore, tests and simulations conducted with only a single LTU in operation confirm that M_y is subject to less structural coupling compared to F_z and M_x. This behaviour is attributed to the vertical force each LTU exerts on the other, which, due to the lateral offset of the LTU's centre of gravity, induces a lateral moment M_x.

Overall, the model accurately predicts the M_y moment. An exception is observed for the front rotor at rotor speeds above 50%, where the experimental confidence intervals are significantly wider than those at lower speeds. As mentioned earlier, this discrepancy is likely attributed to unmodeled structural dynamics within the support structure.

Figure 12 presents the measured and simulated mean and standard deviation of the vertical dynamic acceleration at each LTU location as functions of the rotor speed.

The plot shows that the overall trend is captured by the simulation. The model accurately captures the peak acceleration near 90% rotor speed, although it predicts the maximum at a slightly higher speed. This discrepancy is likely due to a combination of factors, including a slight overestimation of the beam's out-of-plane bending frequency and minor inconsistencies in rotor speed estimation between the experimental and numerical data.

Additionally, the model tends to overestimate both the mean and standard deviation of the acceleration peaks observed around 50% rotor speed, which may be due to an inaccurate representation of the mode shape of the supporting structure excited at this frequency.

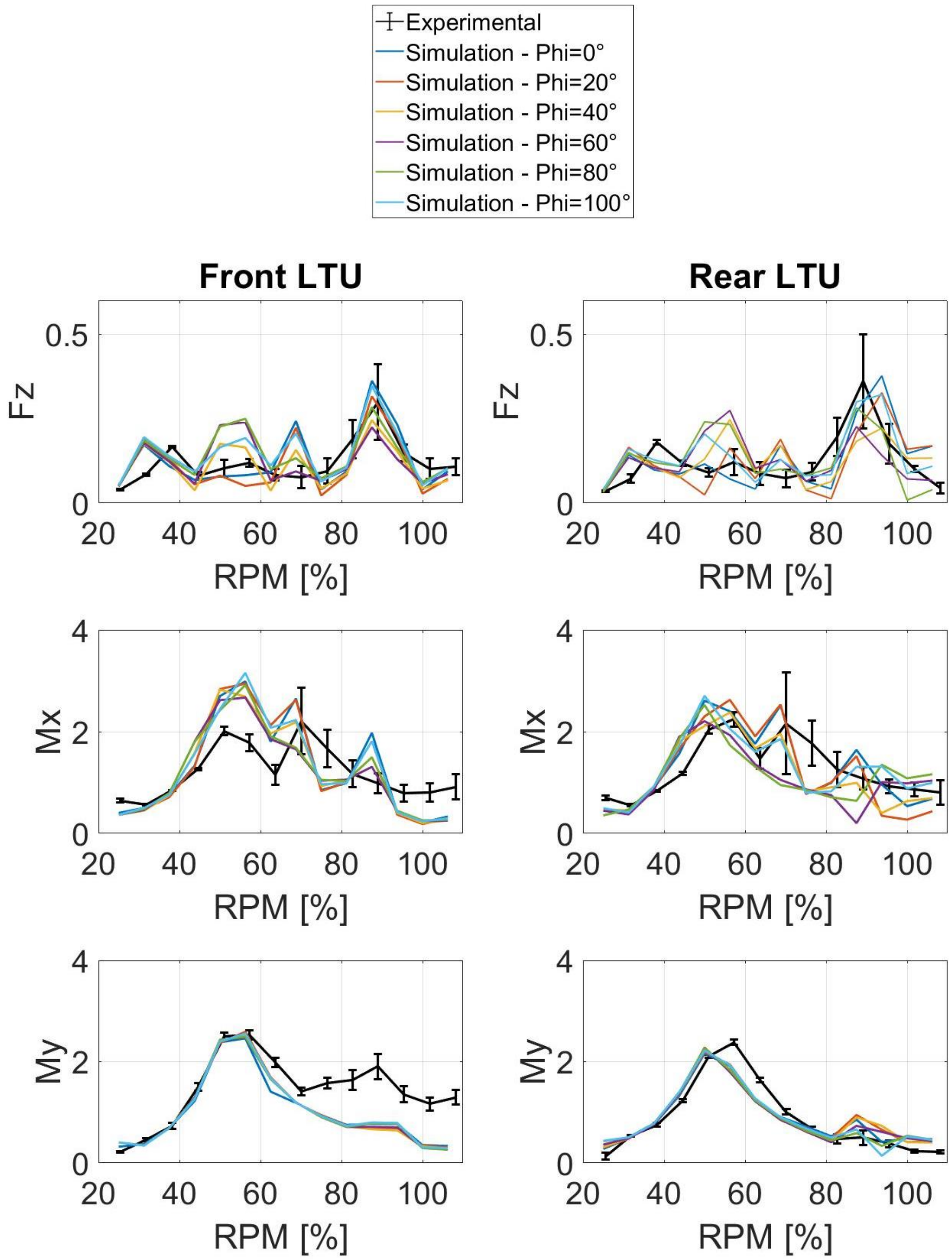

Figure 11: Vertical dynamic forces and moments as functions of rotor speed: measured (black line) and simulated LTUs supported by the elastic beam-pylon model with different front and rear rotor phases.

.

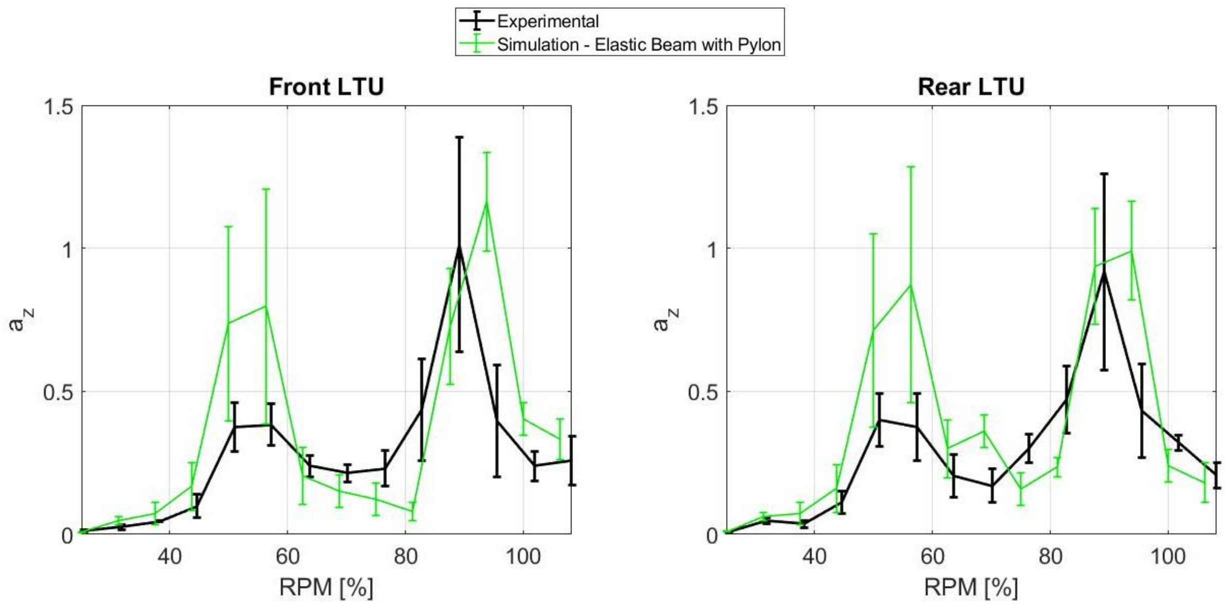

Figure 12: Mean and standard deviation of the vertical dynamic acceleration as functions of rotor speed: measured (black line) and simulated LTUs supported by the elastic beam-pylon model with different front and rear rotor phases (green line).

6. CONCLUSIONS

This paper presented the initial results from wind tunnel testing of two electrical LTUs mounted on a flexible support and the correlation of their dynamic behaviour with aeroelastic models. Using roving hammer tests and operational modal analysis, a representative structural model of the LTU support system was developed. A comparison was conducted between experimentally measured dynamic loads and predictions from models of increasing levels of fidelity. In addition, the influence of the relative rotor phase was investigated.

The following conclusions can be drawn:

1. The dynamic loads experienced by the LTU support structure are influenced by both the structural dynamics of the support system and the dynamic behaviour of the rotors.

   To evaluate the dynamic loads, a detailed model of the LTUs' support structure is essential. Indeed, its introduction proved effective in improving the correlation for all the rotor speeds and load components. The correlation of the vertical acceleration demonstrated its ability in predicting the correct acceleration levels.
2. Accurate evaluation of dynamic loads requires a detailed structural model of the LTU support. The inclusion of such a model was shown to significantly improve correlation across all rotor speeds and load components. In particular, the vertical acceleration predictions demonstrated the model's ability to capture the correct magnitude of the response.
3. The relative phase between multiple LTU rotors has a substantial impact on the resulting dynamic loads transmitted to the structure.
4. These results demonstrate that high dynamic loads can be generated when LTUs with rigid propellers are subjected to edgewise airflow. The loads transmitted at the LTU attachment points can be significantly amplified by the structural dynamics of the supporting system and by the relative phase between rotors. The oscillatory components of these loads are comparable in magnitude to the static components, potentially resulting in elevated vibration levels. Such high dynamic loads may substantially affect the sizing and maintainability of both the LTU and its supporting structure. Therefore, these effects should be considered from the early stages of design, as they can critically influence key aspects of the aircraft architecture, including control strategies, rotor design, and LTU integration.

Appendix A

This Appendix presents the first four mode shapes identified through Experimental Modal Analysis (EMA), along with the corresponding normalized frequencies and damping ratios.

Mode 4, Norm. Frequency: 0.20, Damping Ratio 9.90 [%]

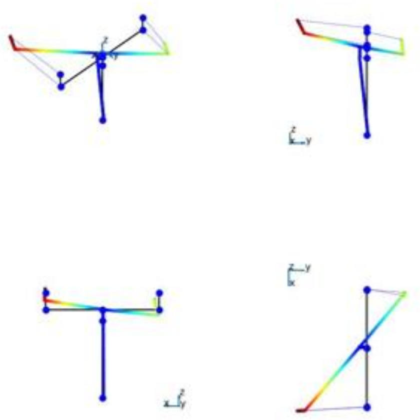

Mode 7, Norm. Frequency: 0.56, Damping Ratio 3.00 [%]

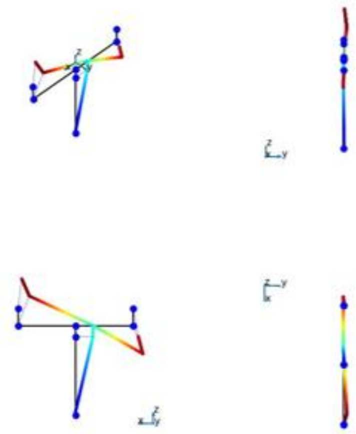

Mode 11, Norm. Frequency: 0.88, Damping Ratio 1.60 [%]

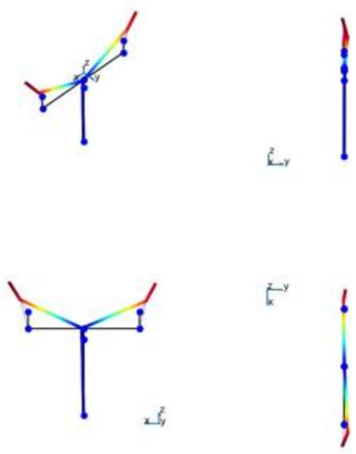

Mode 3, Norm. Frequency: 0.18, Damping Ratio 2.00 [%]

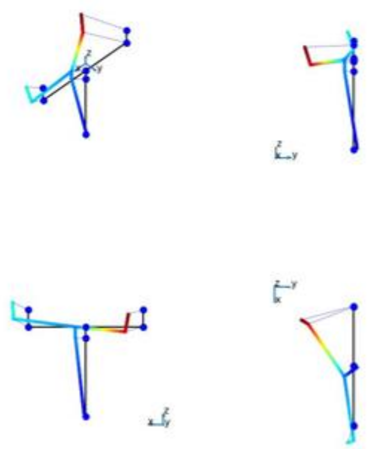

REFERENCES

1. Johnson, W., and Silva, C., “NASA Concept Vehicles and the Engineering of Advanced Air Mobility Aircraft.” *The Aeronautical Journal*, Vol. 126, (1295), 2022, pp. 59–91.
2. Welstead, J. R., “Exploration of Design Drivers for the RVLT Lift+Cruise Reference Vehicle”. NASA TM 20230011630, 2023.
3. Staruk, W., Butt, L., Hennig, G., Bonny, E., Gray, C., Represa, D., & Toner, R., “Wind Tunnel Testing and Analysis of a Rigid, Variable Speed Rotor for eVTOL Applications” *Journal of American Helicopter Society*. Vol. *68,* (3), 2023, 32003-32012
4. Conley, S., Multirotor Test Bed Load and Stress Analysis. NASA TM 20230000313, 2023.
5. Sekula, M.K., & Russell, C.R., Time-Frequency Analysis of Hub Loads in Variable-Speed Rotors. *The Vertical Flight Society's 78th Annual*

Forum & Technology Display, Fort Worth, TX, 10-12 May 2022.

6. Shastry, A., and Datta, A. (2020). Predicting Wake and Structural Loads in RPM-Controlled Multirotor Aircraft. V*ertical Flight Society Aeromechanics for Advanced Vertical Flight Technical Meeting, San Jose, CA*, Jan. 2020

7. Atte, A., Wylie, D., and Rauleder, J., "Experimental Evaluation of Multi-Rotor Aerodynamic Interactions *The Vertical Flight Society's 78th Annual Forum & Technology Display,* Fort Worth, TX, 10-12 May 2022.

8. Russell, C.R., and Conley, S. (2022). The Multirotor Test Bed – A New NASA Test Capability. *The Vertical Flight Society's 78th Annual Forum & Technology Display,* Fort Worth, TX, 10-12 May 2022.

9. Conley, Sarah, and Carl Russell. "Mechanical Design of the Multirotor Test Bed." *Vertical Flight Society Aeromechanics for Advanced Vertical Flight Technical Meeting, San Jose, CA*. 2020.

10. Conley, Sarah, et al. "An Experimental Investigation of Quadrotor Variations using NASA's Multirotor Test Bed. *The Vertical Flight Society's 81st Annual Forum & Technology Display*. 2025.

11. Zilletti, M., D. Prederi, R. Costantini, M. Zaccara, M. Ricciardi, G. Morelli, and P. Masarati. "Wind Tunnel Test of a Single Electrical Lift Thrust Unit to Assess Static and Dynamic Loads." 49th European Rotorcraft Forum, Bueckeburg, Germany, 5-7 Sept., 2023

12. Balatti, D., Zilletti, M., Duina, A., Zaccare, M., Dispenza, A., Masarati, P., "Wind tunnel test of two electrical lift thrust units to assess static and dynamic loads", 50th European Rotorcraft Forum, Marseille, France, 10-12 Sept., 2024

13. Sabatino, E., Prederi, D., Petri, F., Sciarappa, A., Cassinelli, C., Frassoldati, G., " Validation of a flexible and highly scalable mid-fidelity aerodynamic solver with wind-tunnel testing", Vertical Flight Society 79th Annual Forum Proceedings, West Palm Beach, FL, May 2023.

14. Bathe, K.-J. (2014). "Finite Element Procedures" (2nd ed.). Watertown, MA: Klaus-Jürgen Bathe. Chapters 8.3–8.4, pp. 755–758.

15. M. Guskov, J.-J. Sinou, and F. Thouverez, "Multi-dimensional harmonic balance applied to rotor dynamics," *Mechanics Research Communications*, vol. 35, no. 4, pp. 537–545, 2008.

16. Schenk, O., & Gärtner, K. (2004). "Solving unsymmetric sparse systems of linear equations with PARDISO". *Journal of Future Generation Computer Systems*, 20(3), 475–487.

17. Van Overschee, P.; De Moor, B.L.; Hensher, D.A.; Rose, J.M.; Greene, W.H.; Train, K. Subspace Identification for the Linear Systems: Theory–Implementation-Application; Katholieke Universiteit Leuven: Leuven, Belgium; Kluwer Academic Publishers: Boston, MA, USA, 1996